Atmospheric
Measurement
Techniques

# Accounting for surface reflectance spectral features in TROPOMI methane retrievals

**Alba Lorente, Tobias Borsdorff, Mari C. Martinez-Velarte, and Jochen Landgraf**

SRON Netherlands Institute for Space Research, Leiden, the Netherlands

**Correspondence:** Alba Lorente (a.lorente.delgado@sron.nl)

**Abstract.** Satellite remote sensing of methane ($CH_4$) using the TROPOspheric Monitoring Instrument (TROPOMI) aboard the Copernicus Sentinel-5 Precursor (S5-P) satellite is key to monitor and quantify emissions globally. Overall, the S5-P methane data are of satisfying quality, demonstrated by the product validation with ground-based measurements from the Total Carbon Column Observing Network (TC-CON). However, analysis of TROPOMI dry-air column mixing ratio ($XCH_4$) data has pointed to a few false methane anomalies up to 20–40 ppb that can potentially be misinterpreted as enhancements due to strong emission sources. These artefacts are caused by spectral features of the underlying surfaces of specific materials (e.g. carbonate rocks), which are not well represented in the forward model of the retrieval algorithm. In this study we show that the observed anomalies are due to the surface model which describes the spectral dependence of the Lambertian albedo by a second-order polynomial in wavelength. By analysing the ECOSTRESS library that contains laboratory spectra for different types of surfaces, we find that a quadratic function might not be the most optimal representation of the surface reflectance spectral dependencies in the short-wave infrared (SWIR) range. Already the use of a third-order polynomial improves the methane data such that the anomalies disappear at several locations (e.g. Siberia, Australia and Algeria) without affecting the data quality elsewhere, and the quality of the fit significantly improves. We also found that the known bias in retrieved methane for low-albedo scenes slightly improves, but still, a posterior correction needs to be applied, leaving open the question about the root cause of the albedo bias. After applying the adjusted surface model globally, we perform the routine validation with TCCON and Greenhouse gases Observing SATellite (GOSAT) data. GOSAT comparison does not significantly improve, while TCCON validation results show a small improvement in some stations of 2–4 ppb, up to a factor of 10 smaller than the artificial $XCH_4$ enhancements. This reflects that TCCON stations are not close to any of the corrected artefacts, hinting at a limitation of the current validation approach of the S5-P $XCH_4$ data product.

## 1 Introduction

Methane ($CH_4$) obtained from TROPOspheric Monitoring Instrument (TROPOMI) measurements has been crucial to monitor and quantify greenhouse gas emissions worldwide at global, regional and local scales (e.g. Qu et al., 2021; Chen et al., 2022; Sadavarte et al., 2021) and from multiple sources (e.g. Maasakkers et al., 2022; Shen et al., 2022; Lunt et al., 2019). The methane operational retrieval algorithm has provided data with high quality since the satellite instrument was launched in 2017 (Sha et al., 2021). The algorithm has been improved in the last few years to better correct for biases from low-albedo scenes, update the spectroscopy and the regularization in the inversion, and retrieve methane from measurements over the ocean under sun-glint geometry (Lorente et al., 2021, 2022a).

However, intercomparison between different scientific retrieval algorithms (Lorente et al., 2022b) and the systematic analysis of TROPOMI methane data have pointed to biases linked to surface features that lead to false methane anomalies or artefacts (e.g. Barré et al., 2021). These artefacts can be misinterpreted as atmospheric signatures due to emissions by strong methane super-emitters if they are found in e.g. active oil and gas areas or due to processes related to global warming (e.g. Froitzheim et al., 2021). In order to under-

stand and to have an accurate quantification of methane emissions, it is important to correct for these artefacts on an algorithm level. Recently, Jongaramrungruang et al. (2021) analysed the impact of spectrally complex features on retrieved methane abundances and how they could be mitigated by the choices related to instrument and retrieval parameters. Based on the fact that surface materials have specific spectral dependencies of their surface albedo, they showed that using larger-order polynomials could reduce the retrieval biases related to surface features.

In this study, we show that increasing the order of the polynomial that models the surface reflectance spectral dependence in the TROPOMI methane retrieval algorithm removes large localized methane artefacts and improves the resulting spectral fit. We analyse the impact on global methane abundances and assess the quality of the dataset after applying the improved scheme to 4 years of TROPOMI measurements. Applying the improved surface model globally, we perform the routine validation with Total Carbon Column Observing Network (TCCON) and Greenhouse gases Observing SATellite (GOSAT) observations.

## 2   Surface reflectance in RemoTeC

The methane total column-averaged dry-air mole fraction (XCH$_4$) is retrieved from TROPOMI measurements ($y$) of sunlight backscattered by the earth's surface and the atmosphere in the near-infrared (NIR, 757–774 nm) and short-wave infrared (SWIR, 2305–2385 nm) spectral bands. We use the RemoTeC full-physics algorithm (described in detail by Hu et al., 2016, and Lorente et al., 2021) that simultaneously retrieves the amount of atmospheric methane and the physical scattering properties of the atmosphere. The forward model ($F$) employs the LINTRAN V2.0 radiative transfer model in its scalar approximation to simulate atmospheric light scattering and absorption in a plane-parallel atmosphere (Schepers et al., 2014; Landgraf et al., 2001).

The retrieval algorithm aims to find the state vector $x$ that contains CH$_4$ partial sub-column number densities by solving the minimization problem:

$$\hat{x} = \min_x \left( \left\| \mathbf{S}_y^{-1/2} \left( F(x) - y \right) \right\|^2 + \gamma \left\| \mathbf{W} \left( x - x_a \right) \right\|^2 \right), \quad (1)$$

where $\|\cdot\|$ describes the Euclidian norm, $\mathbf{S}_y$ is the measurement error covariance matrix that contains the noise estimate, $\gamma$ is the regularization parameter, $\mathbf{W}$ is a diagonal unity weighting matrix, and $x_a$ is the a priori state vector (Hu et al., 2016). The retrieval state vector contains CH$_4$ partial sub-column number densities at 12 equidistant pressure layers, the total columns of the interfering absorbers CO and H$_2$O, the effective aerosol total column, size and height parameter of the aerosol power law distribution, and the spectral shift and fluorescence in the NIR band. A Lambertian surface albedo in both the NIR and SWIR spectral ranges and their spectral dependence as a polynomial are also retrieved.

Surface reflectance spectral dependence in RemoTeC is modelled using a low-order polynomial in wavelength. The coefficients of the polynomial are elements of the atmospheric state vector to be inferred in the inversion (Eq. 1). The operational retrieval algorithm (up to version 02.03.01) uses a second-order polynomial (Hu et al., 2016), but for specific surfaces this representation is not optimal, and retrieved XCH$_4$ shows enhancements that can be up to 20–40 ppb and that are strongly correlated with surface features. Figure 1 shows an example of an artificial XCH$_4$ enhancement over Siberia where high XCH$_4$ values coincide with a feature of outcrops of Paleozoic carbonate rocks (Froitzheim et al., 2021), recognizable in the Landsat imagery provided by Google Earth. Here, the surface is a type of carbonate rock for which the reflectance has a characteristic spectral feature. Even though this artefact can be mistaken by enhancements produced by underlying methane emissions (Froitzheim et al., 2021), the fact that these enhancements are constant in time and with a shape that does not change with meteorological (e.g. wind) conditions supports the hypothesis that it is an artefact, as reported by Barré et al. (2021).

To improve the characterization of the surface reflectance dependency with wavelength in RemoTeC, following Jongaramrungruang et al. (2021), we look at the ECOSTRESS spectral library (Meerdink et al., 2019), which contains laboratory spectra of minerals, rocks and man-made materials. Analysing the spectral information for different types of surfaces, particularly for rock and concrete, we find that a quadratic function might not be the most optimal representation of the surface reflectance spectral dependencies in the SWIR range. We thus increase the order of the polynomial and analyse the modelled radiance and residuals for the artefact over Siberia. We find that using a third-order polynomial is enough to capture the specific spectral features that cause the localized enhancements and so improves the spectral quality fit. However, outside of this area the fit does not improve, reflecting that a second-order polynomial is optimal to capture the spectral dependencies of most surfaces. Increasing the order of the polynomial to degrees higher than 3 does not further improve the retrieval in any of the cases, producing artificial signals in some of the retrieved parameters and worsening the quality of the fit outside of the specific areas. These findings are also confirmed for other areas with artificial XCH$_4$ enhancements.

### 2.1   Results

Based on our findings, we retrieve 4 years of XCH$_4$ from TROPOMI measurements using a cubic function for the spectral dependence of the Lambertian albedo in the 2.3 μm spectral range to better characterize the surface reflectance spectral features. The updated retrieval algorithm used to retrieve this TROPOMI XCH$_4$ scientific data product was im-
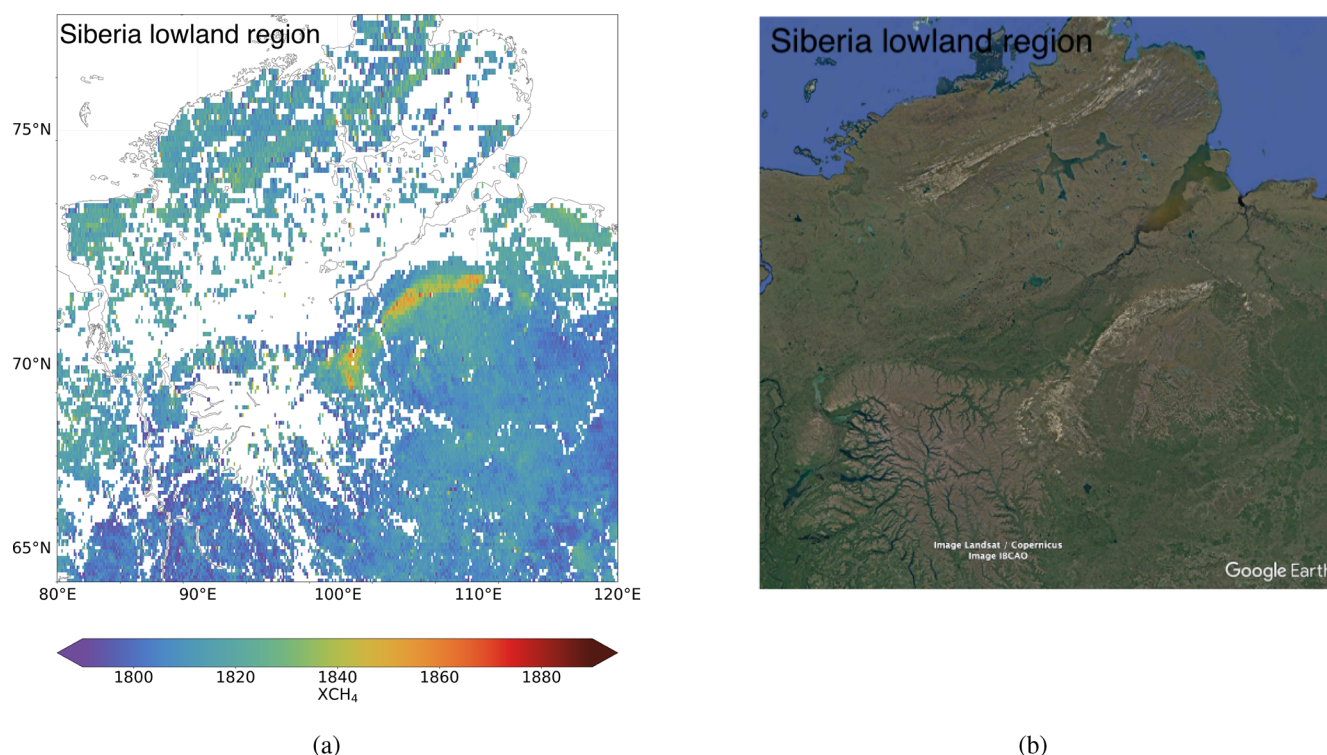
Figure 1. (a) TROPOMI XCH$_4$ retrieved over the North Siberian Lowland region (64–77° N, 80–120° E) averaged from March 2019–March 2020 to a 0.1° × 0.1° grid and (b) Landsat imagery provided by Google Earth © Google, 2022.

plemented in the operational processing algorithm in July 2022 under version 02.04.00. This version of the algorithm has been used for the full mission reprocessing performed by ESA that will be completed before the end of the first quarter of 2023. In this section, we show that with the updated treatment of surface reflectance several artificial XCH$_4$ features are removed, and we analyse the quality of the dataset on the local, regional and global scale.

### 2.1.1 Localized features

Figure 2a shows the fitted SWIR radiance modelled with the forward model using a quadratic and a cubic function to characterize the spectral features of the surface reflectance for one of the pixels that show strong XCH$_4$ enhancement over Siberia (Fig. 1). For this specific pixel, the residuals (i.e. difference between modelled and measured radiance) using a quadratic function show a strong dependency with wavelength (Fig. 2b), while for a pixel outside the enhancement the dependency is not significant (not shown). If we increase the order of the polynomial from second to third order, the dependency with wavelength of the residuals is significantly reduced (Fig. 2c). For this specific pixel, retrieved XCH$_4$ is reduced from 1885 to 1847 ppb, and the $\chi^2$ value for the fit is reduced from 53 to 19 when going from second- to third-order polynomial.

Figure 3 shows three examples of a regional TROPOMI XCH$_4$ distribution for which the modified surface model using the third-order polynomial removes artificial XCH$_4$ enhancements. For the Siberia case (first row) TROPOMI XCH$_4$ shows a strong decrease over the outcrop of carbonate rocks (Fig. 3a, b). The average difference in XCH$_4$ is greater than 1 % over the artefact. The fit significantly improves over the specific feature (Fig. 3c), implying that a third-order polynomial can better capture the surface reflectance spectral dependence of the underlying surface. The fact that the fit does not show an improvement outside the distinguishing feature means that a second-order polynomial is a good representation elsewhere.

The second example in Fig. 3 shows a region in northwestern Australia. Again, artificial enhancements are removed when using the cubic function (Fig. 3d, e). Over this particular region, the underlying soil is composed of sedimentary carbonate (Petheram et al., 2018), and the XCH$_4$ enhancement is also strongly correlated with the retrieved aerosol optical depth (not shown), which points to an interference between the surface spectral features and the representation of scattering processes in the forward model. An erroneous description of the surface reflectance is compensated by enhanced aerosol load, which enhances the atmospheric light path, leading to an overestimation in XCH$_4$. This XCH$_4$ enhancement could be misinterpreted as caused by emissions due to coal mining in the area. However, ap-
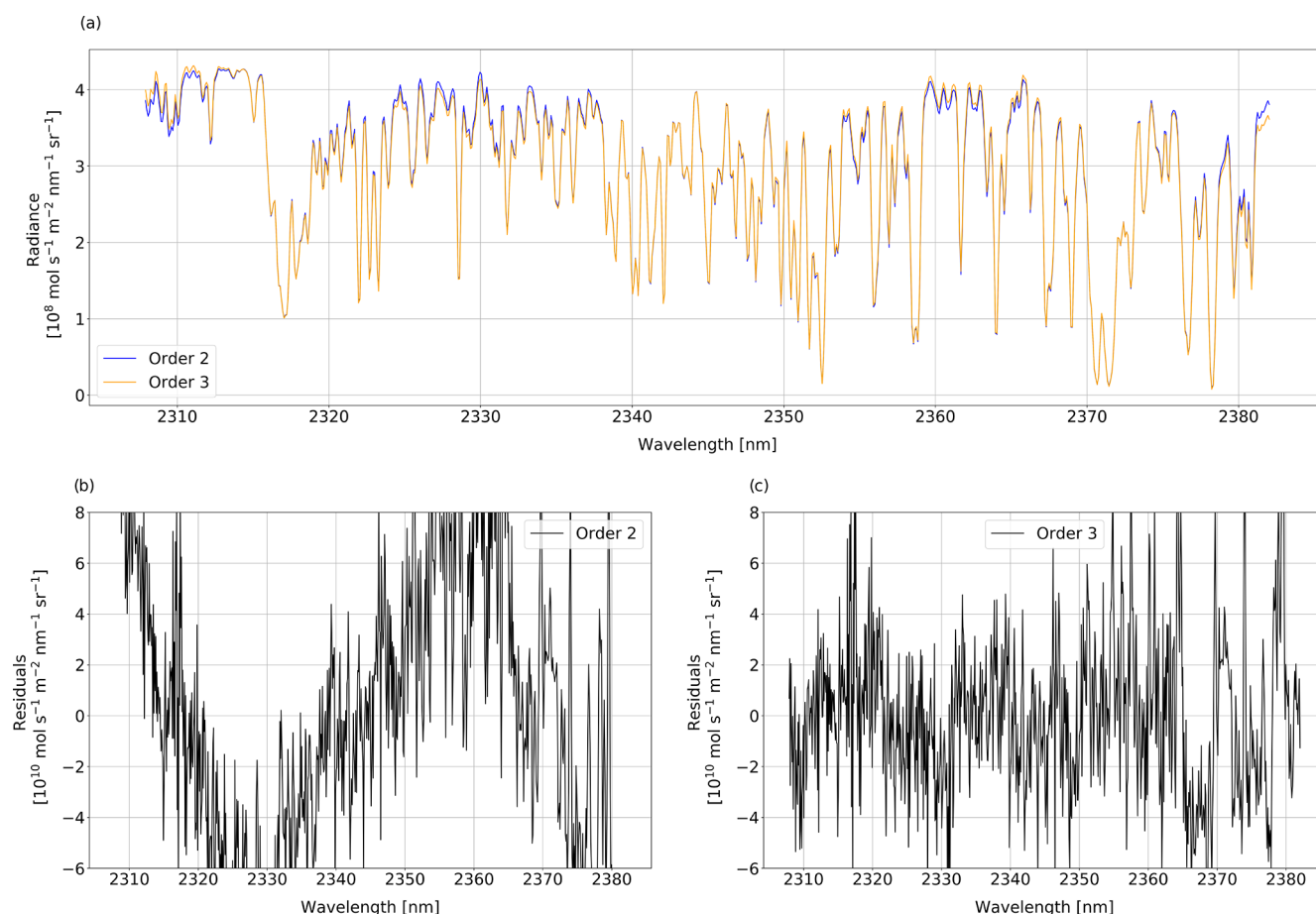
**Figure 2. (a)** Radiance modelled with RemoTeC with a second- and third-order polynomial to characterize the surface reflectance spectral features and **(b, c)** the respective residuals (modelled minus measured radiance) for a pixel (523 369) in orbit 9147 over Siberia.

plying a third-order polynomial removes the localized $XCH_4$ enhancement, and the fit significantly improves over the distinct feature.

The third example of Fig. 3 shows multiple artefacts over north-western Algeria and eastern Tunisia that are removed when using the third-order polynomial. Over this region, land cover is mostly bare rock and soil with some sparse grassland in the north. $XCH_4$ artefacts are correlated with different types of surfaces, some of them being rock and soil composed mostly of carbonate and limestone minerals (Jones et al., 2013). Methane emissions from the oil and gas sector have been actively monitored over these regions using TROPOMI data, so removing the artefacts is extremely relevant to correctly pinpoint $CH_4$ emitters. The Hassi R'Mel oil and gas field is just on the edge of one of the artefacts that has been removed with the new retrieval scheme ($\Delta XCH_4$ plot in Fig. 3h). $XCH_4$ signals from plumes that blow towards the false enhancement because of specific wind conditions might get diffused within the enhancement and are therefore most probably classified as artefacts by plume-detection algorithms due to the high correlation with albedo. Hassi Mes-

saoud is another major oil and gas field from which plumes are detected. It is located in areas where the change in $XCH_4$ by the updated retrieval is not significant; therefore emission estimates from the field should not be affected. In the case of area emission estimation, the effect of the updated retrieval will depend on how the artefacts and uncertainty on the observations are characterized on the inversion schemes. As overall retrieved $XCH_4$ is lower for the country of Algeria, estimated regional emissions with the new retrieval scheme may also be lower.

### 2.1.2 Regional and global effect

Next we analyse at regional and global scales the effect of the adjusted surface model to characterize surface spectral features. Figure 4 shows $XCH_4$ over Asia retrieved with a second- and third-order polynomial, their ratio, and the SWIR surface albedo. The ratio shows clearly localized artefacts that are removed, for example, in several points in the Tibetan Plateau, and also over Siberia, as discussed in the previous section. Overall, the retrieved $XCH_4$ is more homogeneous, particularly over high latitudes. Over the low-
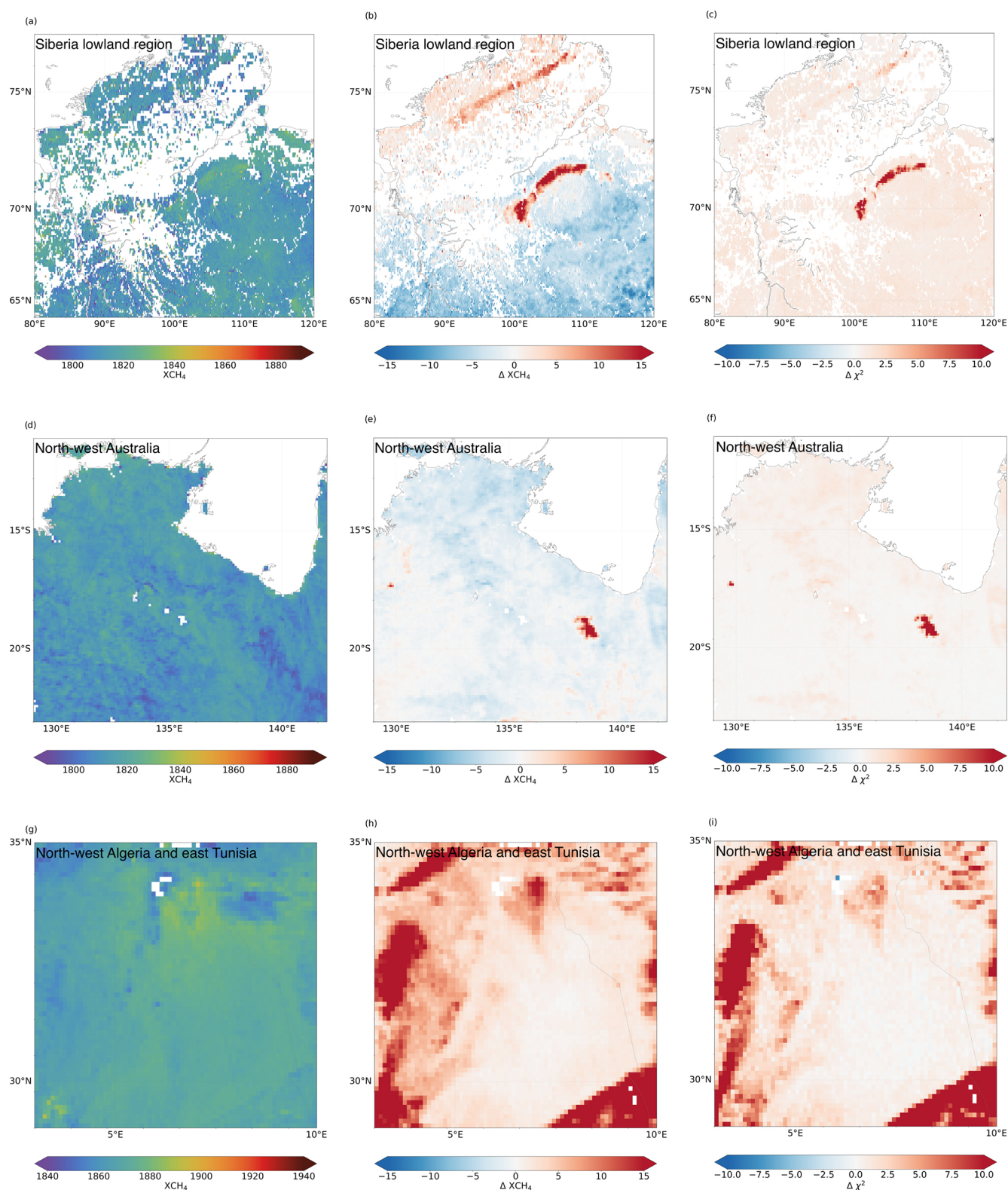
**Figure 3.** (a, d, g) TROPOMI XCH$_4$ retrieved with the third-order polynomial to characterize the surface spectral features; (b, e, h) XCH$_4$ difference that shows XCH$_4$ retrieved with second-order polynomial minus XCH$_4$ retrieved with third-order polynomial; and (c, f, i) difference between $\chi^2$ value for the fit with second- minus third-order polynomial over (first row) the Siberian lowland region (64–77° N, 80–120° E), (second row) north-western Australia (11–23° S, 129–148° E), and (third row) north-western Algeria and eastern Tunisia (29–35° N, 3–10° E), averaged from March 2019–March 2020 to a 0.1° × 0.1° grid.

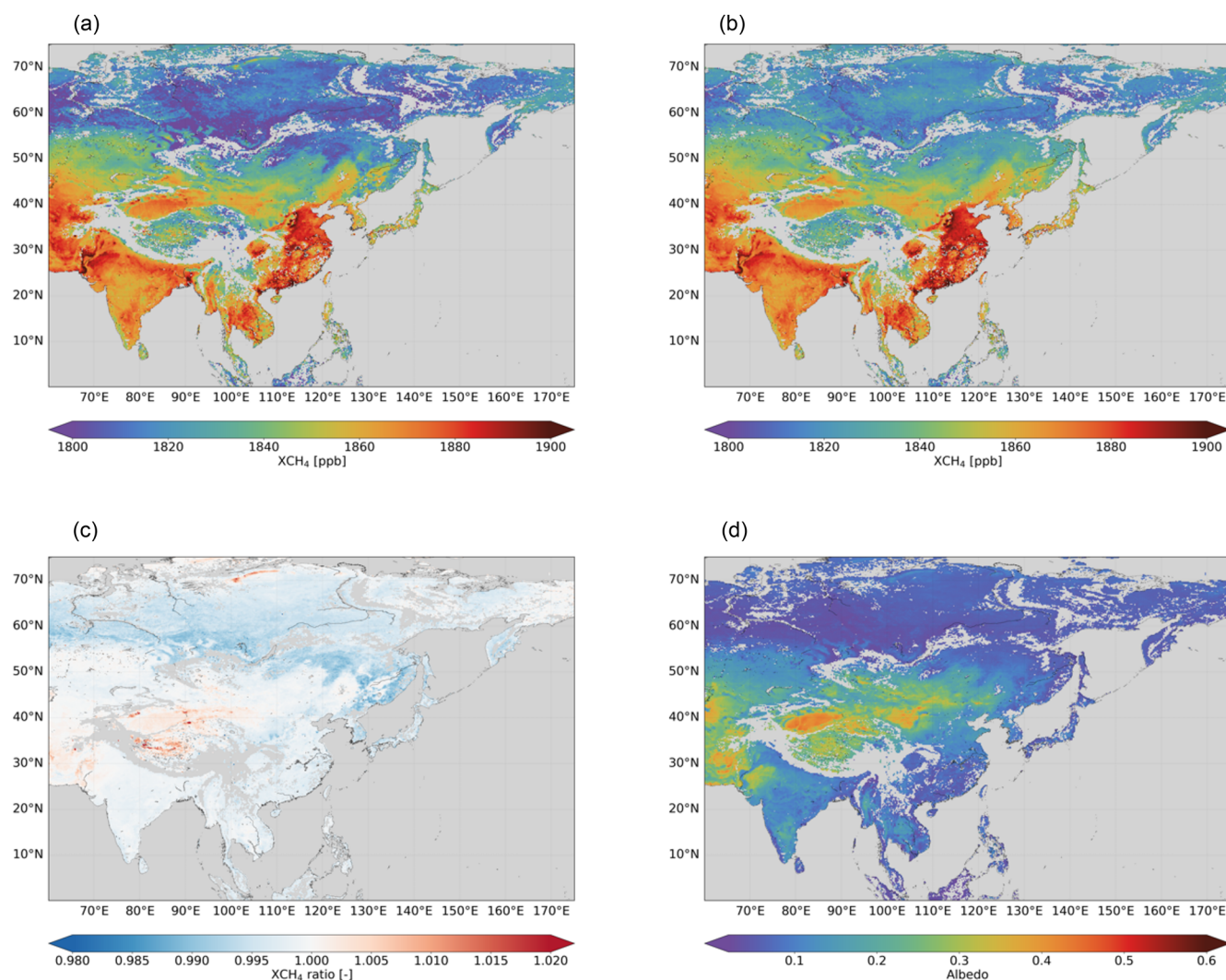**Figure 4.** TROPOMI XCH$_4$ retrieved with (**a**) second- and (**b**) third-order polynomial to characterize the surface spectral features, (**c**) the ratio between XCH$_4$ retrieved with second- and third-order polynomial, and (**d**) the retrieved surface albedo in the SWIR. Daily means in a 0.2° × 0.2° grid are averaged from September 2018–September 2020.

surface-albedo band around the 60° N latitude region, retrieved XCH$_4$ is higher using a third-order polynomial function.

Similar effects can be seen over North America (Fig. 5). Localized artefacts on the northern part of the Delaware Basin are removed: this is relevant in order to attribute sources to individual locations in such large basins as the Permian using TROPOMI observations. Over the Interior Plains of Canada and the area surrounding the Grand Lakes, which are characterized by low surface albedo in the SWIR spectral band, retrieved XCH$_4$ is higher in the new data product, as well as in the western part of the United States.

TROPOMI XCH$_4$ shows an underestimation in areas with low surface albedo retrieved in the SWIR spectral range, for which we apply a posterior correction based on the "small-area approximation" (Lorente et al., 2021). When using the

third-order polynomial to characterize surface spectral features in the forward model, the increase in retrieved XCH$_4$ over the low-albedo regions reduces the low XCH$_4$ bias. We define the bias as the ratio of a reference XCH$_4$ value estimated for albedo values around 0.2 and the retrieved XCH$_4$, following the approach in Lorente et al. (2021). Figure 6 shows the XCH$_4$ bias as a function of surface albedo for XCH$_4$ retrieved using the second- and third-order polynomial. The reduction of the XCH$_4$ bias is significant for albedos below 0.1, up to 1 % for the lowest albedo values of 0.02. However, there is still a dependence of the retrieved XCH$_4$ on albedo that we correct for. This implies that there is an additional error source which causes the albedo biases that needs to be further investigated.
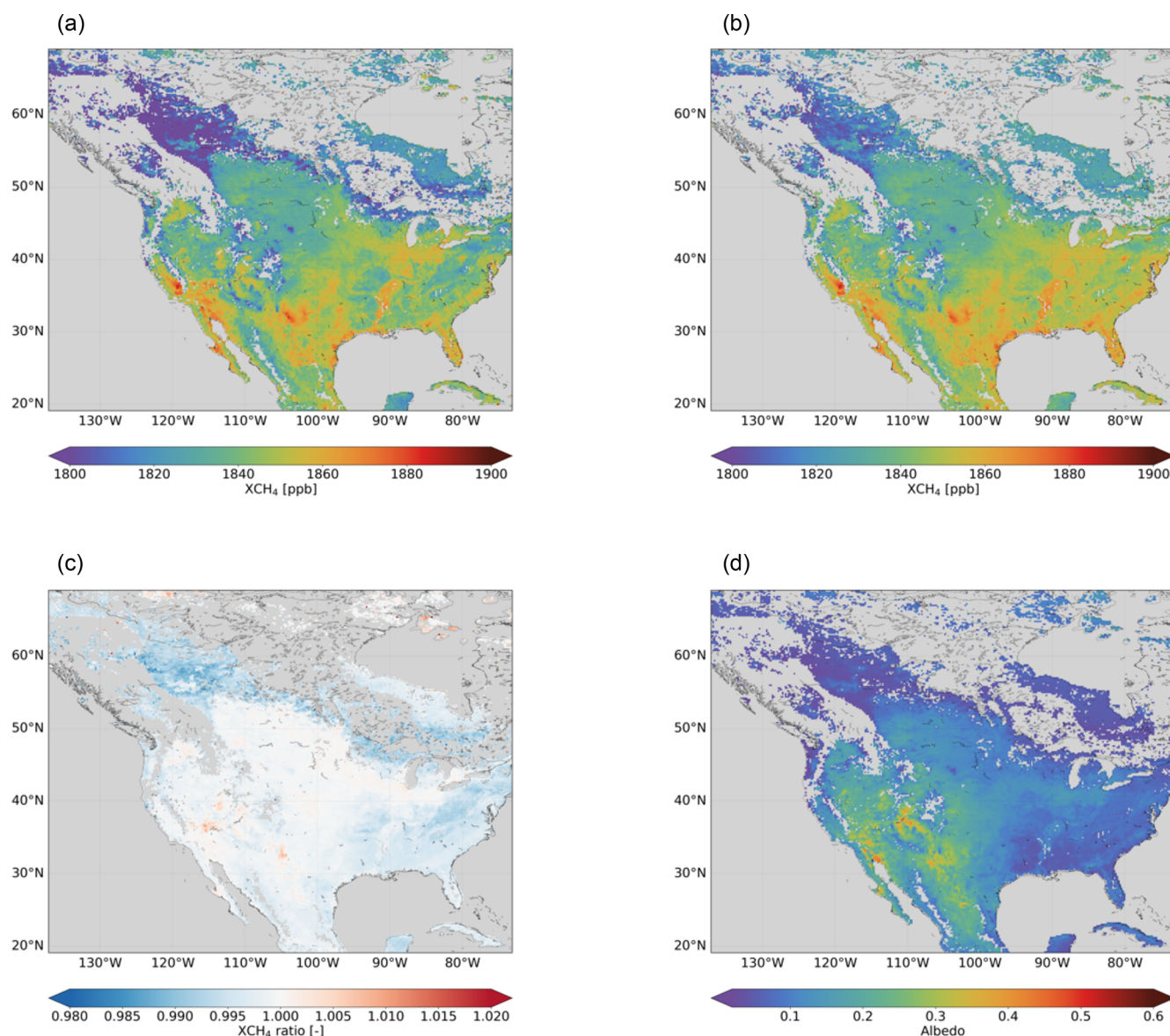
**Figure 5.** TROPOMI $XCH_4$ retrieved with **(a)** second- and **(b)** third-order polynomial to characterize the surface spectral features, **(c)** the ratio between $XCH_4$ retrieved with second- and third-order polynomial, and **(d)** the retrieved surface albedo in the SWIR. Daily means in a $0.2° \times 0.2°$ grid are averaged from September 2018–September 2020.

## 2.2 Validation

To assess the overall quality of the dataset, we perform the routine validation following Lorente et al. (2021, 2022a) using ground-based measurements from the TCCON and measurements from the GOSAT satellite.

### 2.2.1 TCCON

We validate the TROPOMI $XCH_4$ dataset with ground-based measurements from the Total Carbon Column Observing Network (TCCON) (Wunch et al., 2011) (data version GGG2014, downloaded on 15 December 2021). TROPOMI $XCH_4$ is collocated with a spatial radius of 300 km around each station and a temporal overlap of 2 h for the ground-based measurement and the satellite overpass. We average TROPOMI $XCH_4$ and compare it to the TCCON $XCH_4$, and for all individual paired collocations the mean bias of TROPOMI–TCCON $XCH_4$ differences and its standard deviation is estimated. Then, we compute the average of the biases of all stations and its standard deviation as a measure of the station-to-station variability as a diagnostic parameter for the regional bias, following the approach in Lorente et al. (2021).

**Table 1.** Overview of the validation results of TROPOMI XCH$_4$ land measurements with measurements from the TCCON at selected stations. The table shows the number of collocations, mean bias and standard deviation for each station, and the mean bias for all stations, as well as the station-to-station variability. Results are shown for TROPOMI XCH$_4$ with and without the albedo bias correction applied.

| Site, country, lat–long coord. (°) | No. of points | Corrected TROPOMI XCH$_4$ and TCCON | | Uncorrected TROPOMI XCH$_4$ and TCCON | |
| --- | --- | --- | --- | --- | --- |
| | | Bias (ppb, %) | Standard deviation (ppb, %) | Bias (ppb, %) | Standard deviation (ppb, %) |
| Pasadena (US, 34.14, −118.13) | 699 | −5.5 (−0.3) | 9.3 (0.5) | −1.0 (0.0) | 9.3 (0.5) |
| Saga (Japan, 33.24, 130.29) | 276 | 6.6 (0.3) | 13.4 (0.7) | −10.1 (−0.5) | 13.7 (0.7) |
| Karlsruhe (Germany, 49.1, 8.44) | 295 | −3.5 (−0.2) | 9.5 (0.5) | −15.8 (−0.9) | 10.0 (0.5) |
| Darwin (Australia, −12.46, 130.93) | 198 | −10.7 (−0.6) | 12.9 (0.7) | −17.6 (−1.0) | 13.4 (0.7) |
| Wollongong (Australia, −34.41, 150.88) | 423 | −6.4 (−0.4) | 11.5 (0.6) | −11.7 (−0.6) | 11.6 (0.6) |
| Lauder II (New Zealand, −45.04, 169.68) | 358 | −2.9 (0.1) | 11.3 (0.6) | −13.2 (−0.7) | 11.2 (0.6) |
| Park Falls (US, 45.94, −90.27) | 582 | −7.2 (−0.4) | 13.3 (0.7) | −22.6 (−1.2) | 16.1 (0.9) |
| East Trout Lake (Canada, 54.36, −104.99) | 491 | −5.9 (−0.3) | 14.8 (0.8) | −21.8 (−1.1) | 16.6 (0.9) |
| Lamont (US, 36.6, −97.49) | 664 | −10.4 (−0.6) | 8.7 (0.5) | −15.8 (−0.8) | 9.7 (0.5) |
| Orléans (France, 47.97, 2.11) | 390 | −4.5 (0.2) | 11.9 (0.6) | −15.3 (−0.8) | 13.8 (0.7) |
| Edwards (US, 34.95, −117.88) | 757 | 0.4 (−0.0) | 8.9 (0.5) | 4.1 (0.2) | 9.1 (0.5) |
| Sodankylä (Finland, 67.37, 26.63) | 356 | −13.8 (−0.7) | 17.3 (0.9) | −34.2 (−1.8) | 17.8 (1.0) |
| Mean bias, station-to-station variability | | −5.3 (−0.3) | 5.1 (0.3) | −14.6 (−0.8) | 9.5 (0.5) |
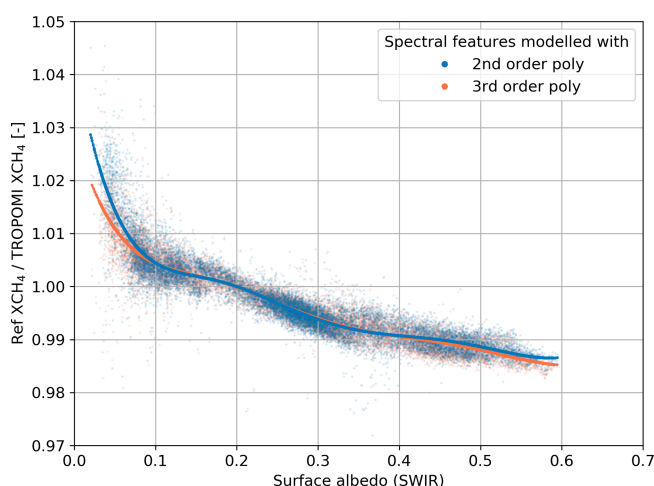


**Figure 6.** Ratio of reference XCH$_4$ to TROPOMI XCH$_4$ as a function of the retrieved surface albedo for TROPOMI XCH$_4$ retrieved using a second- (blue) and third-order (orange) polynomial to model the spectral surface features.

The mean bias is below 1 % for all stations; the validation results are summarized in Table 1. The average bias for all stations is −0.3 % (−5.3 ppb), and the station-to-station variability is 0.3 % (5.1 ppb); both parameters are below the mission requirements of precision and accuracy below 1 % for TROPOMI XCH$_4$ retrievals. Compared to the uncorrected TROPOMI XCH$_4$ (e.g. without the albedo bias correction applied), the mean bias is reduced from −0.8 % to −0.3 %.

Figure 7a shows the mean bias and the standard deviation for each of the stations, and Fig. 7b shows the correlation plot.

These validation results are of similar magnitude to the validation of TROPOMI XCH$_4$ retrieved using a second-order polynomial (e.g. average bias of −5.4 ppb (−0.3 %) and station-to-station variability of 5.1 ppb (0.3 %); Lorente et al., 2022a). TCCON suggests an improvement of around 2–4 ppb in the bias and station-to-station variability when increasing to a third-order polynomial in the surface model. As the biggest changes with the new configuration occur at very localized scales, the improvement in the validation is small compared to the XCH$_4$ decrease over the enhancements. TCCON stations are typically located over homogeneous and spectrally smooth surfaces, and none of the stations are close to any of the detected artefacts and, therefore, cannot capture the most significant changes in retrieved XCH$_4$. This deficit of the TCCON representativeness adds to the lack of coverage for high-albedo regions and over the tropics, already pointed out by Guerlet et al. (2013) and Reuter et al. (2013) when trying to estimate regional uncertainty in satellite-retrieved CO$_2$ concentrations.

### 2.2.2 GOSAT

In this section, we use XCH$_4$ measurements by the Thermal And Near infrared Sensor for carbon Observation – Fourier Transform Spectrometer (TANSO–FTS) on board the Greenhouse gases Observing SATellite (GOSAT) satellite for the validation of TROPOMI XCH$_4$ data. We use the GOSAT proxy XCH$_4$ data product produced at the Netherlands Institute for Space Research (SRON) in the context of
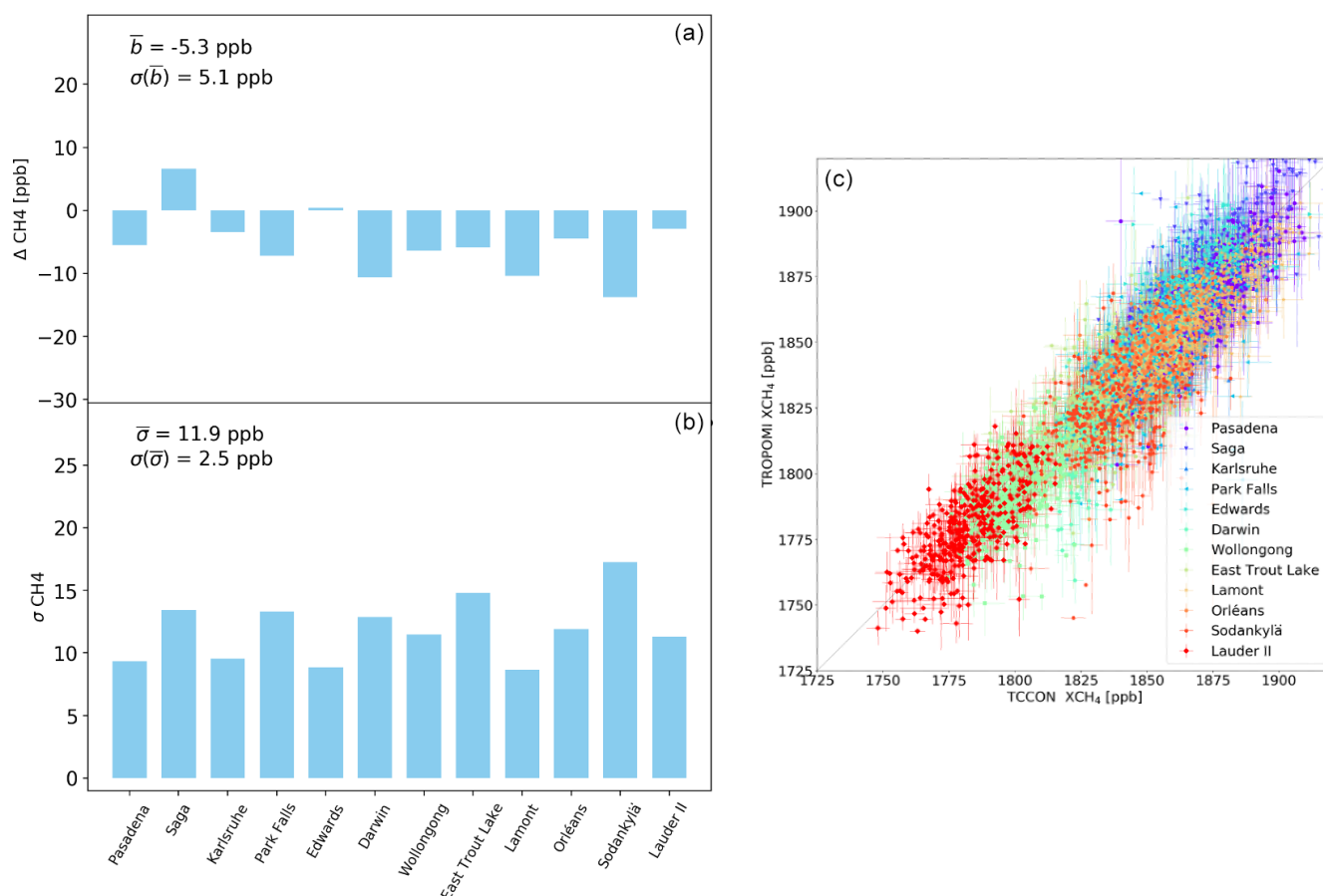
**Figure 7. (a)** Mean differences between TROPOMI and TCCON XCH$_4$ ($\Delta$XCH$_4$) and the standard deviation of the differences ($\sigma_{\mathrm{XCH}_4}$) for each of the stations selected for the validation. **(b)** Correlation of daily average XCH$_4$ measured by TROPOMI and TCCON for all the stations. TROPOMI XCH$_4$ with the albedo bias correction applied is shown.

the ESA GreenHouse Gas Climate Change Initiative (GHG-CCI) project (Buchwitz et al., 2019, 2017). This XCH$_4$ product is retrieved using the RemoTeC proxy retrieval algorithm.

We compare XCH$_4$ retrieved from TROPOMI and GOSAT measurements for the period of March 2018–December 2020, and we compute the average of daily biases and its standard deviation between TROPOMI and GOSAT measurements gridded in a $2° \times 2°$ grid. Globally on average, TROPOMI XCH$_4$ is lower than GOSAT XCH$_4$. The comparison leads to a bias after correction of $-14.4 \pm 15.9$ ppb ($-0.7 \pm 0.8$ %) and a Pearson's correlation coefficient of 0.87.

Similarly to the TCCON validation results, the comparison results for GOSAT are of similar magnitude to the comparison of TROPOMI XCH$_4$ retrieved using a second-order polynomial (e.g. $-13.8 \pm 16.1$ ppb ($-0.7 \pm 0.8$ %); Lorente et al., 2022a). This again reflects the fact that the biggest changes in retrieved TROPOMI XCH$_4$ using the adapted surface model in the retrieval happen at localized scales. Due to the GOSAT-reduced coverage compared to that of TROPOMI and the coarse grid used in the compari-

son, the effect on retrieved TROPOMI XCH$_4$ is not reflected in the TROPOMI to GOSAT comparison.

## 3 Conclusions

The aim of the study was to improve the characterization of the surface reflectance spectral features in the forward model of the TROPOMI XCH$_4$ retrieval algorithm. In the last few years, studies that analysed TROPOMI methane data, as well as an intercomparison between different scientific retrieval algorithms, pointed to a few false methane anomalies linked to features of the underlying surfaces. These anomalies can be misinterpreted as caused by emission sources (e.g. Froitzheim et al., 2021). We have shown that increasing the order of the polynomial that models the surface reflectance spectral dependence in the TROPOMI methane retrieval algorithm removes large localized methane artefacts and improves the resulting spectral fit.

Surface reflectance spectral dependence in the full-physics RemoTeC retrieval algorithm is modelled using a low-order polynomial in wavelength. Analysing the spectral informa-

tion of distinct materials from the ECOSTRESS spectral library, we found that a quadratic function (i.e. second-order polynomial) was not optimal to represent the surface reflectance spectral dependencies of surface materials such as rock and concrete in the SWIR spectral range. In the particular case of the artefact over Siberia, where the underlying surface is composed mainly of carbonate rock, we find that the residuals for specific pixels over the strong XCH$_4$ artefact have a strong dependency with wavelength. When increasing the order of the polynomial that characterizes the surface reflectance spectral dependency in the forward model from second to third, this dependency of the residuals was significantly reduced.

With the improved forward model, we showed that the artificial localized XCH$_4$ enhancements found in several locations like Siberia, Australia and Algeria were caused by surface reflectance spectral features. Some of the artefacts were located close to regions with known emissions due to oil, gas and coal extraction activities, so they could be easily misinterpreted as caused by "real" methane sources. The use of a third-order polynomial removed these artificial XCH$_4$ enhancements and significantly improved the fit over these specific features. Outside the specific features, the spectral fit did not show such substantial improvements, reflecting the fact that a second-order polynomial is sufficient to capture the spectral dependencies of most surfaces, given the characteristics of TROPOMI. We also tested increasing the order of the polynomial to higher degrees, but the retrieved parameters showed undesired behaviour outside the specific areas where the XCH$_4$ artefacts were found, including a worsening of the spectral fit. Based on these results, we apply the third-order polynomial for the surface reflectance spectral dependency globally.

The analysis at regional and global scales of the effect of using the improved characterization of the surface spectral features shows that over low-surface-albedo areas (e.g. regions around the 60° N latitude on the Asian continent) retrieved XCH$_4$ is higher. As a consequence, the known bias in retrieved XCH$_4$ for low-albedo scenes slightly improves, but still, a posterior correction needs to be applied. This implies that even if the bias for scenes with low albedo becomes weaker, there is still an error source which causes systematic albedo biases that needs to be further investigated.

Finally, we assess the quality of the dataset after applying the third-order polynomial, performing the routine validation with TCCON and GOSAT. GOSAT comparison does not significantly improve, while TCCON validation results show an improvement in some stations of 2–4 ppb, significantly smaller than the artefacts that can be as high as 20–40 ppb. The reason is that TCCON stations are typically located around spectrally smooth surfaces, not close to any of the locations where the improved effect has the biggest impacts. This reflects the limitations of the TCCON stations as a validation network, as it does not represent the heterogeneous conditions found by global observing systems like TROPOMI. Given the rapid development of Earth observation technologies, and with several global missions going to be launched in the next decade, validation approaches need to be reassessed to have a reliable system.

# References

Barré, J., Aben, I., Agustí-Panareda, A., Balsamo, G., Bousserez, N., Dueben, P., Engelen, R., Inness, A., Lorente, A., McNorton, J., Peuch, V.-H., Radnoti, G., and Ribas, R.: Systematic detection of local $CH_4$ anomalies by combining satellite measurements with high-resolution forecasts, Atmos. Chem. Phys., 21, 5117–5136, https://doi.org/10.5194/acp-21-5117-2021, 2021.

Buchwitz, M., Reuter, M., Schneising, O., Hewson, W., Detmers, R. G., Boesch, H., Hasekamp, O., Aben, I., Bovensmann, H., Burrows, J., Butz, A., Chevallier, F., Dils, B., Frankenberg, C., Heymann, J., Lichtenberg, G., De Mazière, M., Notholt, J., Parker, R., Warneke, T., Zehner, C., Griffith, D. W. T., Deutscher, N., Kuze, A., Suto, H., and Wunch, D.: Global satellite observations of column-averaged carbon dioxide and methane: The GHG-CCI $XCO_2$ and $XCH_4$ CRDP3 data set, Remote Sens. Environ., 203, 276–295, https://doi.org/10.1016/j.rse.2016.12.027, 2017.

Buchwitz, M., Aben, I., Armante, R., Boesch, H., Crevoisier, C., Di Noia, A., Hasekamp, O. P., Reuter, M., Schneising-Weigel, O., and Wu, L.: Algorithm Theoretical Basis Document (ATBD) – Main document for Greenhouse Gas (GHG: $CO_2$ and $CH_4$) data set CDR 3 (2003–2018), C3S project, Copernicus Climate Change Service, Project number: C3S_D312b_Lot2.1.3.2-v1.0_ATBD-GHG_MAIN_v3.1, 43 pp., https://www.iup.uni-bremen.de/carbon_ghg/docs/C3S/CDR3_2003-2018/ATBD/C3S_D312b_Lot2.1.3.2-v1.0_ATBD-GHG_MAIN_v3.1.pdf (last access: 27 March 2023), 2019.

Chen, Z., Jacob, D. J., Nesser, H., Sulprizio, M. P., Lorente, A., Varon, D. J., Lu, X., Shen, L., Qu, Z., Penn, E., and Yu, X.: Methane emissions from China: a high-resolution inversion of TROPOMI satellite observations, Atmos. Chem. Phys., 22, 10809–10826, https://doi.org/10.5194/acp-22-10809-2022, 2022.

Froitzheim, N., Majka, J., and Zastrozhnov, D.: Methane release from carbonate rock formations in the Siberian permafrost area during and after the 2020 heat wave, P. Natl. Acad. Sci. USA, 118, e2107632118, https://doi.org/10.1073/pnas.2107632118, 2021.

Guerlet, S., Butz, A., Schepers, D., Basu, S., Hasekamp, O. P., Kuze, A., Yokota, T., Blavier, J., Deutscher, N. M., Griffith, D. W., Hase, F., Kyro, E., Morino, I., Sherlock, V., Sussmann, R., Galli, A., and Aben, I.: Impact of aerosol and thin cirrus on retrieving and validating $XCO_2$ from GOSAT shortwave infrared measurements, J. Geophys. Res.-Atmos., 118, 4887–4905, https://doi.org/10.1002/jgrd.50332, 2013.

Hu, H., Hasekamp, O., Butz, A., Galli, A., Landgraf, J., Aan de Brugh, J., Borsdorff, T., Scheepmaker, R., and Aben, I.: The operational methane retrieval algorithm for TROPOMI, Atmos. Meas. Tech., 9, 5423–5440, https://doi.org/10.5194/amt-9-5423-2016, 2016.

Jones, A., Breuning-Madsen, H., Brossard, M., Dampha, A., Deckers, J., Dewitte, O., Gallali, T., Hallett, S., Jones, R., Kilasara, M.and Le Roux, P., Micheli, E., Montanarella, L., Spaargaren, O., Thiombiano, L., Van Ranst, E., Yemefack, M., and Zougmore, R.: Soil Atlas of Africa, Publications Office of the European Union, 176 pp., https://doi.org/10.2788/52319, 2013.

Jongaramrungruang, S., Matheou, G., Thorpe, A. K., Zeng, Z.-C., and Frankenberg, C.: Remote sensing of methane plumes: in-strument tradeoff analysis for detecting and quantifying local sources at global scale, Atmos. Meas. Tech., 14, 7999–8017, https://doi.org/10.5194/amt-14-7999-2021, 2021.

Landgraf, J., Hasekamp, O. P., Box, M. A., and Trautmann, T.: A linearized radiative transfer model for ozone profile retrieval using the analytical forward-adjoint perturbation theory approach, J. Geophys. Res.-Atmos., 106, 27291–27305, https://doi.org/10.1029/2001JD000636, 2001.

Lorente, A., Borsdorff, T., Butz, A., Hasekamp, O., aan de Brugh, J., Schneider, A., Wu, L., Hase, F., Kivi, R., Wunch, D., Pollard, D. F., Shiomi, K., Deutscher, N. M., Velazco, V. A., Roehl, C. M., Wennberg, P. O., Warneke, T., and Landgraf, J.: Methane retrieved from TROPOMI: improvement of the data product and validation of the first 2 years of measurements, Atmos. Meas. Tech., 14, 665–684, https://doi.org/10.5194/amt-14-665-2021, 2021.

Lorente, A., Borsdorff, T., Martinez-Velarte, M. C., Butz, A., Hasekamp, O. P., Wu, L., and Landgraf, J.: Evaluation of the methane full-physics retrieval applied to TROPOMI ocean sun glint measurements, Atmos. Meas. Tech., 15, 6585–6603, https://doi.org/10.5194/amt-15-6585-2022, 2022a.

Lorente, A., Buchwitz, M., Borsdorff, T., and Schneising, O.: Validation Report – SWIR, https://methaneplus.eu/#docs (last access: 14 March 2023), 2022b.

Lorente, A., Borsdorff, T., Martinez Velarte, M. C., and Landgraf, J.: SRON S5P – RemoTeC scientific TROPOMI XCH4 dataset v19_446, Zenodo [data set], https://doi.org/10.5281/zenodo.7766558, 2023.

Lunt, M. F., Palmer, P. I., Feng, L., Taylor, C. M., Boesch, H., and Parker, R. J.: An increase in methane emissions from tropical Africa between 2010 and 2016 inferred from satellite data, Atmos. Chem. Phys., 19, 14721–14740, https://doi.org/10.5194/acp-19-14721-2019, 2019.

Maasakkers, J. D., Varon, D. J., Elfarsdóttir, A., McKeever, J., Jervis, D., Mahapatra, G., Pandey, S., Lorente, A., Borsdorff, T., Foorthuis, L. R., Schuit, B. J., Tol, P., van Kempen, T. A., van Hees, R., and Aben, I.: Using satellites to uncover large methane emissions from landfills, Sci. Adv., 8, eabn9683, https://doi.org/10.1126/sciadv.abn9683, 2022.

Meerdink, S. K., Hook, S. J., Roberts, D. A., and Abbott, E. A.: The ECOSTRESS spectral library version 1.0, Remote Sens. Environ., 230, 111196, https://doi.org/10.1016/j.rse.2019.05.015, 2019.

Petheram, C., Gallant, J., Stone, P., Wilson, P., and Read, A.: Rapid assessment of potential for development of large dams and irrigation across continental areas: application to northern Australia, Rangeland J., 40, 431–449, https://doi.org/10.1071/RJ18012, 2018.

Qu, Z., Jacob, D. J., Shen, L., Lu, X., Zhang, Y., Scarpelli, T. R., Nesser, H., Sulprizio, M. P., Maasakkers, J. D., Bloom, A. A., Worden, J. R., Parker, R. J., and Delgado, A. L.: Global distribution of methane emissions: a comparative inverse analysis of observations from the TROPOMI and GOSAT satellite instruments, Atmos. Chem. Phys., 21, 14159–14175, https://doi.org/10.5194/acp-21-14159-2021, 2021.

Reuter, M., Bösch, H., Bovensmann, H., Bril, A., Buchwitz, M., Butz, A., Burrows, J. P., O'Dell, C. W., Guerlet, S., Hasekamp, O., Heymann, J., Kikuchi, N., Oshchepkov, S., Parker, R., Pfeifer, S., Schneising, O., Yokota, T., and Yoshida,

Y.: A joint effort to deliver satellite retrieved atmospheric $CO_2$ concentrations for surface flux inversions: the ensemble median algorithm EMMA, Atmos. Chem. Phys., 13, 1771–1780, https://doi.org/10.5194/acp-13-1771-2013, 2013.

Sadavarte, P., Pandey, S., Maasakkers, J. D., Lorente, A., Borsdorff, T., Denier van der Gon, H., Houweling, S., and Aben, I.: Methane Emissions from Superemitting Coal Mines in Australia Quantified Using TROPOMI Satellite Observations, Environ. Sci. Technol., 55, 16573–16580, https://doi.org/10.1021/acs.est.1c03976, 2021.

Schepers, D., aan de Brugh, J., Hahne, P., Butz, A., Hasekamp, O., and Landgraf, J.: LINTRAN v2.0: A linearised vector radiative transfer model for efficient simulation of satellite-born nadir-viewing reflection measurements of cloudy atmospheres, J. Quant. Spectrosc. Ra., 149, 347–359, 2014.

Sha, M. K., Langerock, B., Blavier, J.-F. L., Blumenstock, T., Borsdorff, T., Buschmann, M., Dehn, A., De Mazière, M., Deutscher, N. M., Feist, D. G., García, O. E., Griffith, D. W. T., Grutter, M., Hannigan, J. W., Hase, F., Heikkinen, P., Hermans, C., Iraci, L. T., Jeseck, P., Jones, N., Kivi, R., Kumps, N., Landgraf, J., Lorente, A., Mahieu, E., Makarova, M. V., Mellqvist, J., Metzger, J.-M., Morino, I., Nagahama, T., Notholt, J., Ohyama, H., Ortega, I., Palm, M., Petri, C., Pollard, D. F., Rettinger, M., Robinson, J., Roche, S., Roehl, C. M., Röhling, A. N., Rousogenous, C., Schneider, M., Shiomi, K., Smale, D., Stremme, W., Strong, K., Sussmann, R., Té, Y., Uchino, O., Velazco, V. A., Vigouroux, C., Vrekoussis, M., Wang, P., Warneke, T., Wizenberg, T., Wunch, D., Yamanouchi, S., Yang, Y., and Zhou, M.: Validation of methane and carbon monoxide from Sentinel-5 Precursor using TCCON and NDACC-IRWG stations, Atmos. Meas. Tech., 14, 6249–6304, https://doi.org/10.5194/amt-14-6249-2021, 2021.

Shen, L., Gautam, R., Omara, M., Zavala-Araiza, D., Maasakkers, J. D., Scarpelli, T. R., Lorente, A., Lyon, D., Sheng, J., Varon, D. J., Nesser, H., Qu, Z., Lu, X., Sulprizio, M. P., Hamburg, S. P., and Jacob, D. J.: Satellite quantification of oil and natural gas methane emissions in the US and Canada including contributions from individual basins, Atmos. Chem. Phys., 22, 11203–11215, https://doi.org/10.5194/acp-22-11203-2022, 2022.

Wunch, D., Toon, G. C., Blavier, J.-F. L., Washenfelder, R. A., Notholt, J., Connor, B. J., Griffith, D. W. T., Sherlock, V., and Wennberg, P. O.: The Total Carbon Column Observing Network, Philos. T. Roy. Soc. A, 369, 2087–2112, https://doi.org/10.1098/rsta.2010.0240, 2011.